13th EWTEC 2019 Proceedings of the 13th European Wave and Tidal Energy Conference 1-6 Sept. 2019, Naples, Italy

SAND2019-15166C

Predicting the Dynamic Characteristics of a Fully Submerged Wave Energy Converter Subjected to a Power Take-Off Failure using a High-Fidelity Computational Fluid Dynamics Model

Toan T. Tran, Aaron M. Krueger, Budi Gunawan, Mohammad-Reza Alam

Abstract—**In this study, we develop an algorithm to implement the physics of a mooring tether connected to a submerged wave energy converter (WEC). The algorithm, built as a java subroutine, is implemented and tested on a high-fidelity computational fluid dynamic (CFD) code STAR-CCM+. A fluid-structure interaction (FSI) model for a fully submerged buoy absorber WEC connected to a single mooring tether, with an internal fault in the power take-off (PTO) system, is simulated. The PTO fault, i.e. a seized PTO drive shaft or generator short circuit in electrical systems, is being modelled and simulated using the high-performance computing (HPC) clusters at Sandia National Laboratories and University of California Berkeley. The algorithm and simulation results are verified and partially compared to the mid-fidelity open source code, WEC-Sim. The results include dynamic responses of the WEC body, tether tension, and PTO stroke. Based on the simulation results, the significance of a PTO failure event on the WEC integrity is discussed.**

Keywords—**Fully submerged wave energy converter (WEC), Power take-off (PTO) failure, Slack tether, Fluid-Structure Interaction (FSI), WEC-Sim**

I. Introduction

THE development of wave energy converter (WEC) technologies is playing an indispensable role in the emergence of renewable energy technologies. WEC components, including an absorber, power take-off (PTO) machinery, and sub-components needs to be robust and efficient throughout its deployment lifetime to be economically viable. A fault occurrence on the WEC, such as mooring failure, PTO failure, loss of grid power, etc., may result in significant increases of structural and mechanical loads acting of the device that can compromise the structural integrity of the WEC. A number of design standards and guidance propose the use of standard design load cases (DLCs) [1,2]. These DLCs need to model events with device failure to be considered as part of the design and evaluation process for WECs. However, none of the standards and guidance has been widely accepted, mainly due to the lack of practical experience in implementing them. Numerical models often do not have built-in functions or features to model the PTO or mooring lines/tethers. Therefore, custom functions or features often need to be developed specifically for the project.

As slack forms in the tether line, a damaging shock load may occur and be transferred to other WEC subsystems such as structural joints, PTO, etc. Subsequently, this extreme loading can impact the expected lifetime of the whole system [3,4], and cause a PTO failure [5,6]. Therefore, developers should take into account these conditions during the design phase of their WEC.

In this study, a high-fidelity fluid-structure interaction simulation is developed to estimate dynamic loads due to seized PTO condition. A numerical approach is adopted and integrated into computational fluid dynamic (CFD) code to model the physics of PTO-tether dynamics. The presented coupling simulation inherently consists of several advantage features, such as multiphase flow with volume of fluid (VOF) nonlinear wave models, six degree-of-freedoms (6-DOFs) solver and overset grid technique. The simulation result performed by the current coupling approach then is verified and partially compared to the well-known open source code, WEC-Sim [7] and experimental data. Additionally, the CETO WEC model [8] is chosen as a study case for predicting the effect a seized PTO on device loading and behaviour.

II. Numerical Algorithm

The numerical algorithm is implemented in the following test problem. A fully submerged single tether WEC (displayed in Figure 1) simulation models excitation, radiation, hydrostatic/buoyancy, power take off (PTO), and drag forces due to wave motion. The PTO force is numerically estimated from a user defined function,

Paper ID 1392 in WHM Track.

T. Tran was with Department of Mechanical Engineering, University of California Berkeley, CA, USA. He is now with National Renewabe Energy Laboratory (NREL) (email: trantoan2018@berkeley.edu; ThanhToan.Tran@nrel.gov)

R. Alam are with Department of Mechanical Engineering, University of California Berkeley, CA, USA. (email: reza.alam@berkeley.edu)

A. Krueger and B. Gunawan are with Sandia National Laboratories (SNL), Albuquerque, NM, USA. (email: amkrueg@sandia.gov; bgunawa@sandia.gov)

whereas the other forces are internally calculated using the CFD solver.

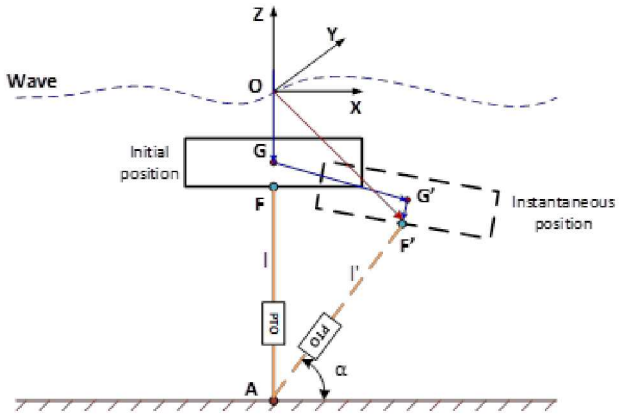

Fig. 1. Schematic showing a kinematic of submerged WEC body motion

For the submerged WEC, the PTO force is induced in the direction of the tether and act against the hydrostatic force. A pretension force acting on PTO exists to counteract the hydrostatic force. As a result of the pretension force, the WEC body is able to neutralize its position below the sea water surface. Since the PTO is directly connected to the tether and the tether stiffness is much larger than that of the PTO, the effect of tether elongation during operational condition is neglected. In the present study, the PTO mechanism is assumed as a linear spring-damper system where its reaction force is given by

$$F_{PTO} = -K_{PTO}\Delta l - C_{PTO}\dot{\Delta l} - |F_h| \tag{1}$$

where the terms of K_{PTO} and C_{PTO} refer to the stiffness and damping of the PTO. The terms Δl and $\dot{\Delta l}$ refer to the relative displacement and velocity motion of the PTO. The term F_h is hydrostatic force, transformed to the tether direction based on the translational and rotational motions of the WEC body.

Figure 1 shows the kinematics of the submerged WEC body motion, which is used to calculate parameters such as location and velocity at the representative attachment point F. These parameters are subsequently used to calculate PTO reaction force on WEC body. The attachment point is assumed as a connection point between the PTO and WEC hull. The connection point between the tether and seabed is located at point A. At any given time in the simulation, the WEC body with a center of gravity (CG) of G is simultaneously translated and rotated to a new location G′. The coordinate system of the updated attachment point F′ is given as below

$$\overrightarrow{OF'} = \overrightarrow{OG} + \overrightarrow{GG'} + \overrightarrow{G'F'} \tag{2}$$

where point O is the origin of the global coordinate system, located at the water surface. As the simulation time progresses the vector $\overrightarrow{G'F'}$ is continuously updated based on the following equation

$$\overrightarrow{G'F'} = T \times \overrightarrow{GF} \tag{3}$$

where T is a rotation matrix defined by the standard 3-2-1 Euler angle theory.

Additionally, the derived velocity vector at the attachment point, $\overrightarrow{V_{F'}}$ is described as follows

$$\overrightarrow{V_{F'}} = \overrightarrow{V_{G'}} + \Omega_{G'} \times \overrightarrow{G'F'} \tag{4}$$

where $\overrightarrow{V_{G'}}$ is a translational velocity at CG and $\overrightarrow{\Omega_{G'}}$ is an angular velocity (ω) matrix, given as

$$\Omega_{G'} = \begin{bmatrix} 0 & -\omega_z & \omega_y \\ \omega_z & 0 & -\omega_x \\ -\omega_y & \omega_x & 0 \end{bmatrix} \tag{5}$$

In the present study we apply the presented algorithm to a single tether-PTO WEC, with the ability to implement multiple tether PTOs.

III. NUMERICAL MODEL SETUP

The semi-implicit time integration method is available in STAR-CCM+, a commercial CFD software. It is used to solve the pressure-linked equations in which the linkage between the momentum and continuity equation is achieved through a predictor-corrector approach. The second-order upwind scheme was applied for the convection term. In unsteady simulations, a second-order central difference scheme was used for temporal discretization. The Shear Stress Transport k-ω turbulence model was applied to resolve the turbulence behaviour in the fluid domain. The all-y+ wall treatment, a hybrid wall treatment, provides reasonable boundary layer characteristics for meshes of intermediate resolution. In addition, an overset-based grid technique was applied to efficiently handle large moving bodies in fluid-structure interaction simulation.

Figure 2 shows the algorithm used to implement the physics of a mooring tether connected to a submerged WEC. The algorithm, built as a Java subroutine, was implemented and tested on the STAR-CCM+. A fluid-structure interaction (FSI) model for a fully submerged buoy absorber WEC connected to single mooring tether, with an PTO system, was simulated using the VOF model in conjunction with the 6-DOFs solver. In each timestep, the Java subroutine was applied internally to track the connection point between tether and WEC body. The 6-DOF solver updated the WEC body position and orientation. Subsequently, the tether tension components were estimated using the numerical algorithm presented in the previous section. The subroutine is able to evaluate several features such as minimum line tension, PTO failure, slack event, and tether breaking event. In this study, the single tether PTO modelled in the CETO 5 [8] device will be utilized as a case study. The PTO failure is

assumed to be occurred during a power production condition. A summary of the CETO 5 model description is shown in Table 1.

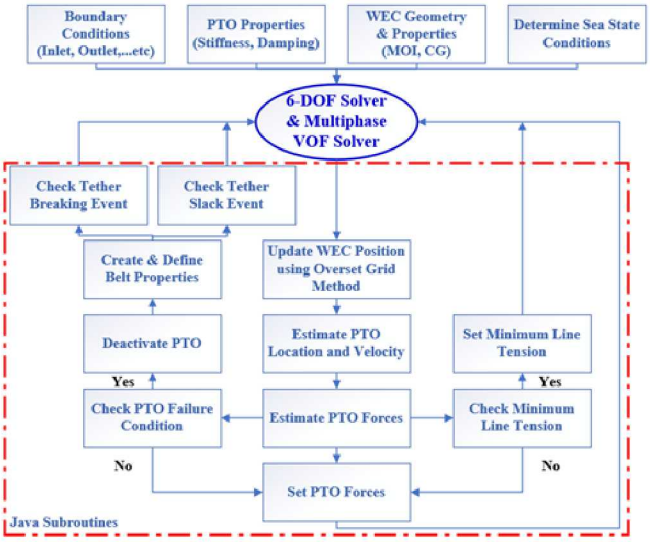

Fig. 2. The PTO implementation algorithm for the submerged WEC with one mooring tether.

Figure 3 shows the numerical wave tank domain of the submerged WEC model based on the overset grid topology. The lengths of the domain upstream and downstream of the WEC were each set to two times the simulated wave length. The width of the domain was set to approximately 13 times the WEC radius. A Cartesian grid was generated using a trimmed cell technique, a method that provides a robust and efficient method of producing a high-quality grid for complex geometry and flow feature resolution. Additionally, a grid refinement was generated around the WEC body and free-water surface regimes so that the complex flow characteristics around the WEC body can be adequately captured. Fifteen logarithmic cell layers, with a first layer thickness of 2.5E-5 m, was used for the near the wall layers around the WEC body. Overall, three different mesh resolutions were generated to assess the convergence of the grid, which is described in detail in the next section.

TABLE I
CETO 5 MODEL DESCRIPTION [8]

Property	Unit	Value
Diameter	m	7
Height	m	5
Displacement	m3	148
Mass of the buoy	kg	35,000
Stroke length	m	6
PTO model	Linear spring-damper	
Spring stiffness	kN/m	150
Damping coefficient	kN/m.s	25
Water density	kg/m3	1,025
Water depth	m	20
Center of gravity	m	-3.5
Stiffness upper end stop spring	kg/m	243,000
Stiffness lower end stop spring	kg/m	215,000

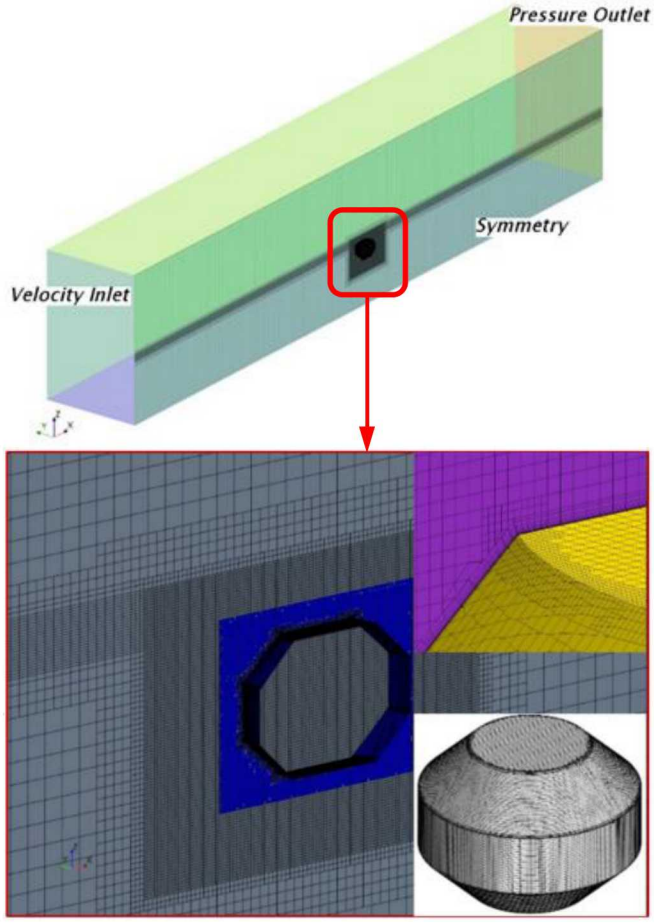

Fig. 3. Computational mesh used in the present study (fine grid resolution).

Figure 3 also depicted the defined boundary conditions of the simulation domain. An inlet velocity was defined at the upstream and bottom boundaries. The pressure outlet was set at the downstream and top boundaries. A fifth-order Stokes wave model was used for generating incident waves via prescribing the velocity at the inlet boundary. Symmetric boundary condition was imposed on the rest of boundary domains. These settings were also applied for floating offshore wind turbine in the previous study [9]. Specially, the wave forcing model which can be used to efficiently damp the upstream-propagating waves at inlet and outlet boundary was applied to perform on a reduced domain. This model reduced the size of the computational domain and thus reduced the computing effort while not compromising the accuracy and reliability of the solution [10]. In addition to reducing the computational domain, the simulations were run on Sandia National Laboratories's (SNL) Skybridge and Chama high performance computers (HPCs) and the University of California Berkeley's (UCB) Savio HPC to decrease the overall simulation time. The simulations run on SNL's HPC required 40 to 80 nodes at 16 cores per node and 64 GB of RAM per node (640 to 1,280 cores and 2.56 to 5.12 TB of RAM) whilst it was run on UCB's HPC with 24 nodes (Intel Xeon E5-2670 v2) at 20 cores and 64 GB of RAM per node. Each simulations approximately took up to one hour to complete one wave period.

IV. VERIFICATION AND VALIDATION

To ensure that the implementation of the tether dynamics is applied correctly a code-to-code comparison and validation studies were completed. The simulations produced using STAR-CCM+ were compared against WEC-Sim [10], a mid-fidelity boundary element model. The STAR-CCM+ simulations were also compared against experimental datasets collected from a scaled WEC model testing.

Based on the CETO 5 model description in Table 1, a STAR-CCM+ simulation and a WEC-Sim simulation were created. The STAR-CCM+ simulation was first compared to WEC-Sim to ensure similar results are achieved, to verify if the tether dynamics is implemented correctly. The STAR-CCM+ simulation results were then compared to experimental data to ensure the wave model matched experimental data as well as or better than mid-fidelity codes such as WEC-Sim. There are three quantities of interest (QoIs) that were observed as a function of time: the normalized tension, surge, and heave of the WEC. These QoIs adequately represent the main data necessary for designing WECs. Figure 4 shows a reasonably good agreement between the STAR-CCM+ simulation, WEC-Sim simulation, and the experiment. Even though the experimental surge and heave was larger than predicted by the STAR-CCM+ simulation, the resulting tether tension was very similar and had better agreement with the experimental results than the WEC-Sim simulation. To quantify if the CFD simulation model setup was better than the WEC-Sim simulation, the L1 norm and L2 norm were calculated. The L1 norm, a calculation of average difference between the experiment and the simulation, and L2 norms, a calculation of average standard deviation between the experiment and the simulation, (Eqs. (6) and (7)) quantified the performance of the two simulations for each quantity of interest (QoI) (e.g. Normalized Tension). As shown in Table 2, the performance of the CFD simulation setup was better than the performance of WEC-Sim for this particular data set. Therefore, the CFD simulation setup is adequate for additional studies.

$$L_1 norm = \frac{\sum_{i=1}^{N}\left(QoI_{Exp,i} - QoI_{Sim,i}\right)}{N} \tag{6}$$

TABLE 2
NUMERICAL COMPARISON USING L1 AND L2 NORMS

Comparison case	Norm	Tension (N)	Surge (m)	Heave (m)
Exp to CFD	L1	0.2411	0.2993	0.2086
	L2	0.2923	0.3485	0.2473
Exp to WEC-Sim	L1	0.7287	1.1984	0.6835
	L2	0.3976	0.6236	0.3501

TABLE 3
COMPUTATIONAL MESH RESOLUTION PROPERTIES

Mesh case	Mesh base size	No. element	Min/Max mesh size on WEC surface	Vertical grid size at water surface regime
Coarse	0.16	1.15 million	0.04/0.08	14
Medium	0.14	1.82 million	0.035/0.70	16
Fine	0.1	3.67 million	0.025/0.50	24

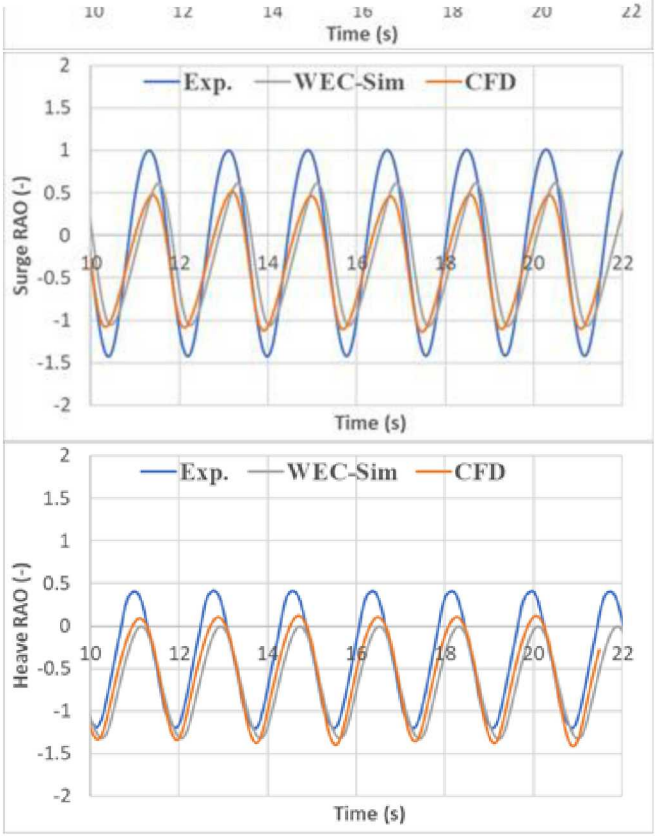

Fig. 4. Validation and verification simulation of submerged WEC system.

$$L_2 norm = \frac{\sqrt{\sum_{i=1}^{N}\left(QoI_{Exp,i} - QoI_{Sim,i}\right)^2}}{\sqrt{N}} \tag{7}$$

To ensure that the mesh did not impact the results, a grid convergence study was completed to assess numerical uncertainty. The mesh resolution properties are listed in Table 3. The mesh was modified by altering the base size based on trimmer mesh approach. This ensured the mesh resolution on WEC surface and refinement regime on water surface was varied accordingly. As shown in Table 3, maximum and minimum mesh size on the WEC surface is constrained by 50% and 25%, respectively. Particularly, the vertical grid size at water surface zone from trough and crest wave location is varied between 14 and 24. A ratio of grid size between horizontal and vertical direction is kept as 4 for all mesh generation in this study. For this study, 320-time steps per wave period numerically satisfied the guideline formulation recommendations [7].

Figure 5 shows the CFD results of the convergence test of grid resolution for the submerged CETO 5 model subject to regular wave condition. Visually, the results seem to be insensitive to the mesh resolution, but to make sure, the grid convergence index (GCI) [11] is calculated using Eq. (3) to determine the numerical uncertainty for each plot in Figure 5 and in Table 4. For each timestep, the GCI was calculated using a factor of safety (F_s) of 3.0, the order-of-accuracy (p) was assumed to be 2.0, the refinement factor was set to the refinement ratio between the most refined mesh and the second most refined mesh, f_1 is the QoI on the most refined mesh, and f_2 is the QoI on the second most refined mesh. The unsteady GCI uncertainty bars are added to the most refined case in Figure 6, which shows that the solution is insensitive to the grid. Base on the grid convergence study, the medium grid which optimally balance accuracy and cost of simulation is selected for further study.

$$GCI_t = F_s \frac{|f_1 - f_2|}{r_{12}^p - 1} \tag{8}$$

TABLE 4
NUMERICAL UNCERTAINTY USING GCI

Norm	WEC Surge (m)	WEC Heave (m)	WEC Rotation (Deg)	Tether Tension (N)
L1	0.0328	0.0410	0.3404	1.162E04
L2	0.0891	0.0560	0.8576	1.7150E04

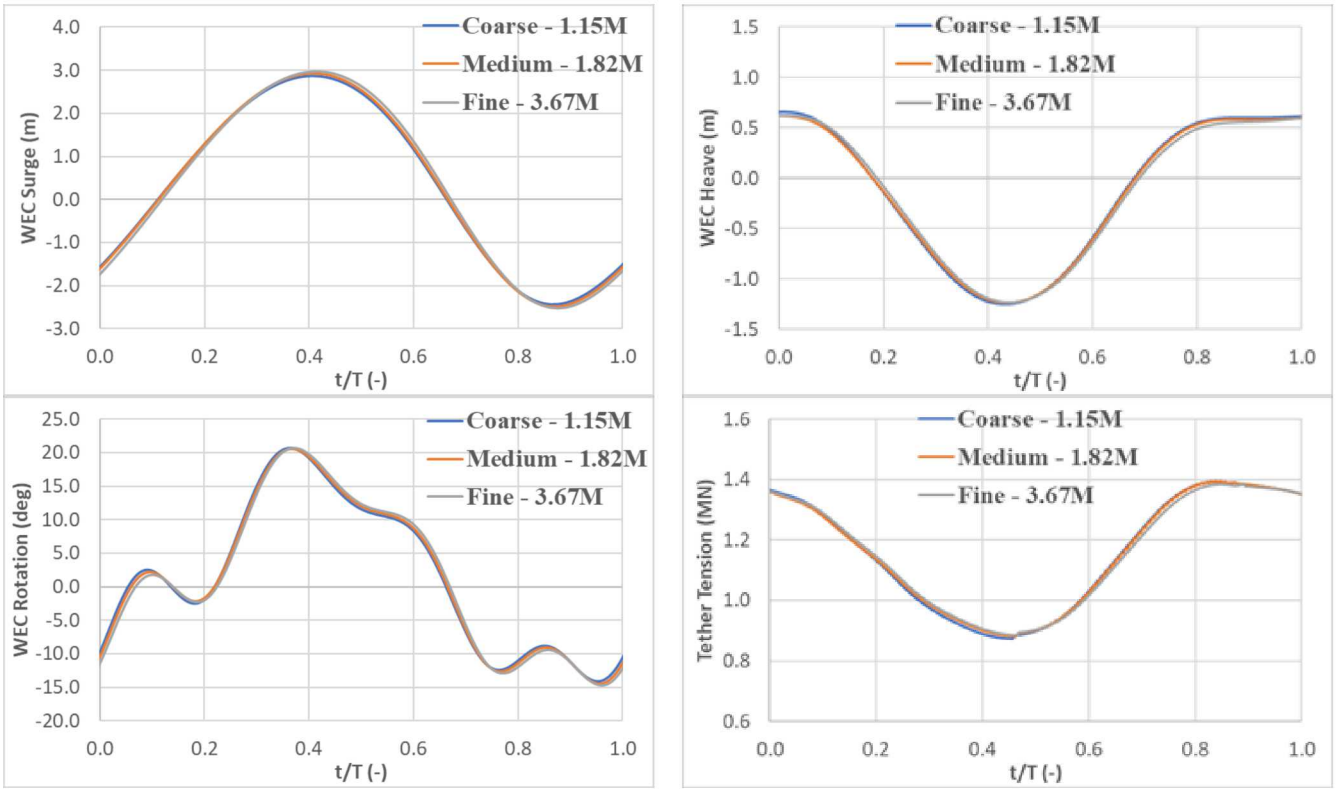

Fig. 5. Unsteady convergence test of grid resolution for fully submerged CETO 5 model.

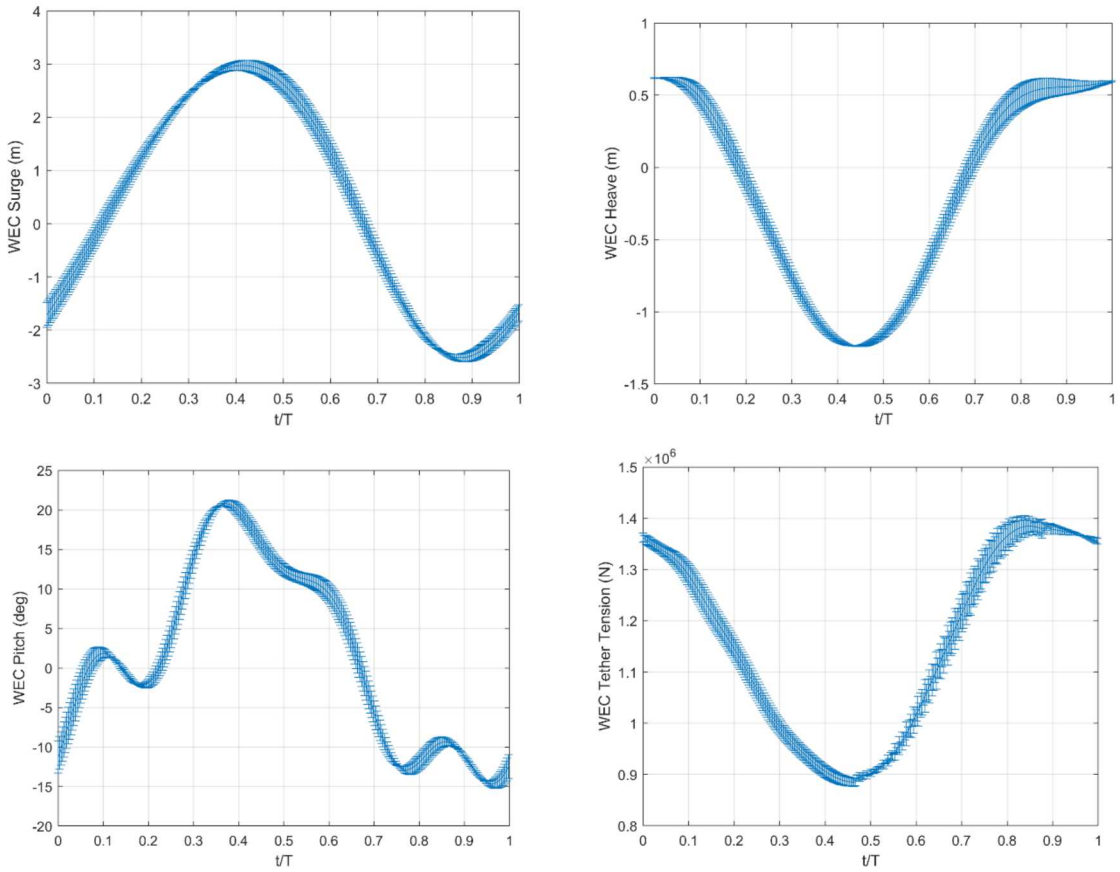

Fig. 6. Unsteady convergence test with uncertainty bars for fully submerged CETO 5 model.

V. Results and Discussion

Design standards require developers to consider system faulty cases, such as a fault in the PTO system during power production, as ones of the design load cases. There are several common fault cases [1,2] during power production, such as transducer failure, specifying incorrect PTO restraint forces, joint seizure in an articulated part of the WEC structure, complete seizure, hydraulic or pneumatic PTO depressurization, etc. These type of faults may have a relatively low probability of occurrence for well-designed systems, but such faults could cause significant consequences, such as accelerated fatigue damages on WEC components. This study focuses on the fault causes by PTO/piston seizure, i.e. when the movement of a piston within a linear PTO becomes heavily restricted due to the seizure.

The CFD simulation was set up to model a PTO seizure condition for the CETO 5 wave energy model [1] under a normal operating condition at the Galway Bay, Ireland, test site. The normal operating condition case was selected based on the records of energy period and significant wave height at Galway Bay from Sep. 2013 to Sep. 2018 [12], shown in figure 7. Since the high occurrence probability of wave condition is relatively well distributed, an operational wave condition with a significant wave height (Hs) of 0.9 m and energy period (Te) of 5 s (or peak wave period, T of 5.82 s) is selected.

Figure 8 shows the converged simulation results that include dynamic responses of the WEC body and tether line tension, before and after a seized PTO event. The ramp up time at the beginning simulation is removed from the plots. The x axis in each plot shows time, normalized by T. The seized PTO event starts at approximately at t/T = 2. Starting at this point of time the tether tension and force start to change rapidly, i.e. at a higher frequency than during normal operation, and more abruptly, which is attributed to the loss of damping in the system. The PTO stroke becomes zero, indicating no movement on the PTO piston. When seized, the PTO system changes from a mass spring-damper system to a mass-spring system, causing the WEC system to oscillate at a higher frequency. At this stage, the system plays as a pendulum which its natural frequency depends on the net buoyancy, tether length and the buoy mass plus added mass. The oscillation frequency is six to seven times higher than that for normal operating conditions. This was confirmed by ploting the power spectral density of the tether forces (Figure 9). This finding indicates that the cyclical loading frequency is also increased by a factor of six to seven, although at the same time the amplitude of the load is decreased. The changes of this dynamic loading behaviour could potentially reduce the fatigue life of the affected WEC components. An in-depth analysis, e.g. using finite element analysis, is needed to quantify the impact of this behaviour change.

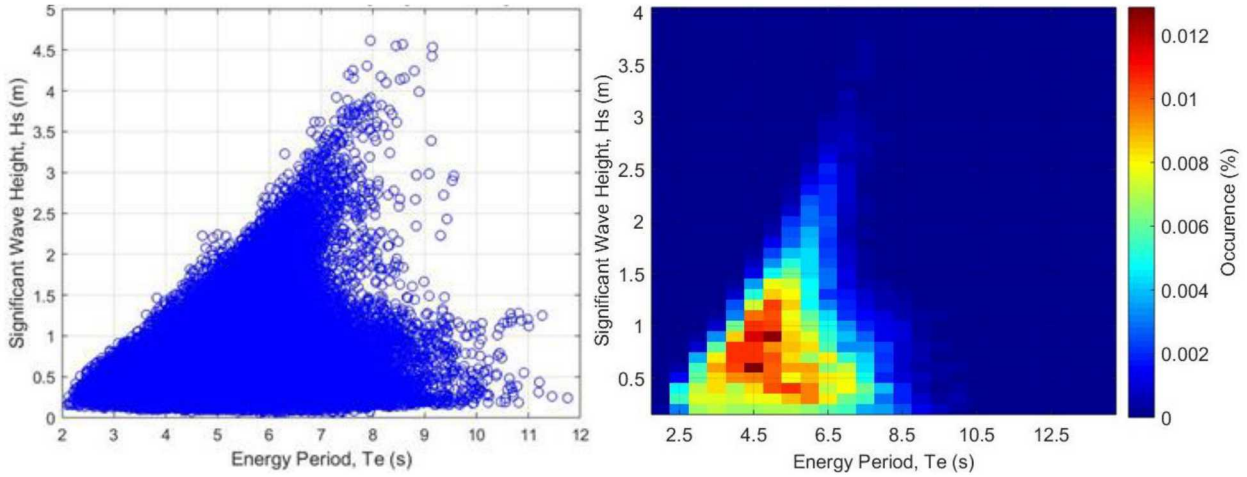

Fig. 7. Wave data and JPD contour at Galway Bay site (Sep. 2013 – Sep. 2018).

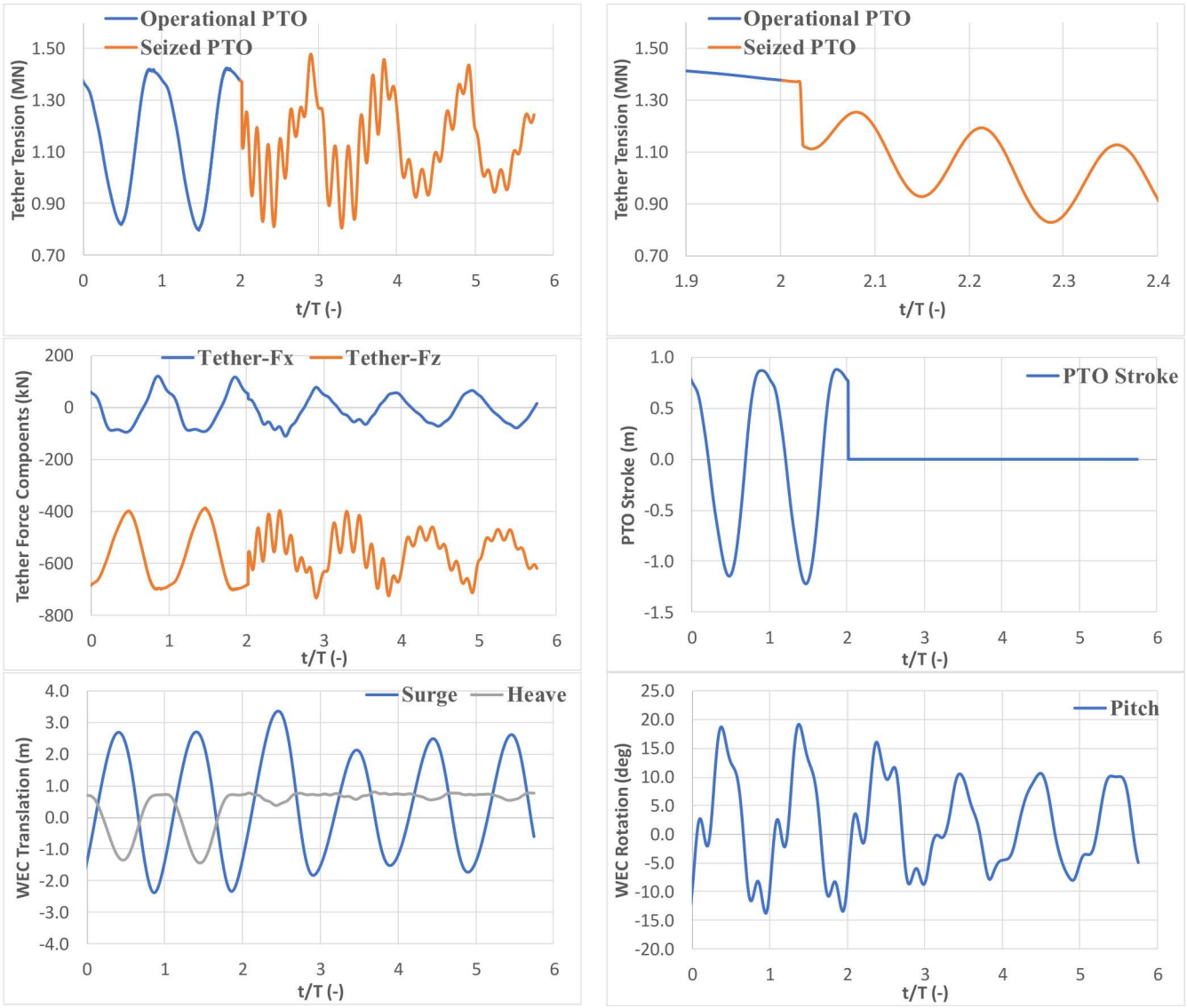

Fig. 8. Tether tension and dynamic responses of WEC body under power production mode with PTO failure condition

In addition, while the higher frequency movement of the system impacts the dynamics of the WEC, the maximum tether forces do not increase significantly. More specifically, the WEC heave displacement stays approximately constant, while the amplitudes of the surge displacement and pitch rotation decrease. When the PTO started to seize, the WEC's vertical position(translation) and PTO stroke were near its maximum range, i.e. z ~ 0.8 m at t/T = 2. Hence, the WEC stays more or less at the same z location after seizure.

In Figure 10, the free-surface evolution of the high-fidelity simulation is depicted for eight different time instants during one wave period for the operational condition. The free-surface is represented by an iso-surface volume of fluid variable calculated from the simulation result. As one can observe, the non-linear wave profile around WEC body is graphicly displayed. Specifically, the WEC body simultaneously moves forward and down (Figure 8), in a clockwise direction. The water surface on the top of the WEC move from trough to crest during the first half of wave period (T_1-T_4). At the same time, it rotates backward. At the time T4, simultaneous WEC body motions including heave, surge, and pitch leads to highly non-linear water surface. At this time, the biggest gap between water surface and WEC top surface can be observed. The higher non-linear wave surface can be found during times T_4-T_6. On the contrary, the WEC body seems to be moved out of water during the rest of wave period (T_4-T_8). It should be noted that the WEC motion during this stage is entire reversal compare to the previous stage (T_1-T_4).

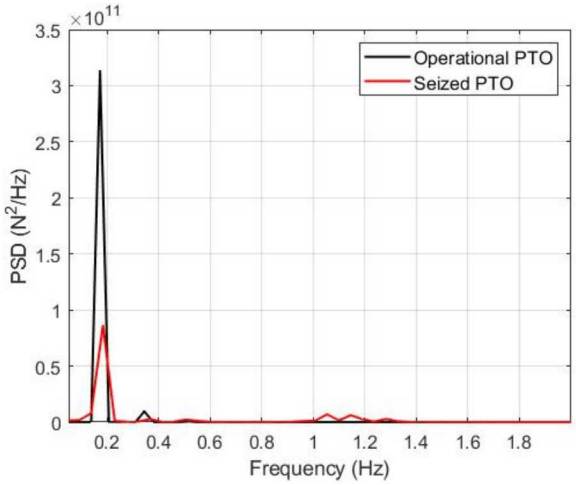

Fig. 9. The power spectral density of the tether tension for operational and seized PTO conditions

VI. Summary and Conclusion

A model to represent the physics of WEC tethers was developed in Java and implemented to a single tether CETO 5 WEC in STAR-CCM+. The model was used to investigate the dynamic behaviours of the WEC when the PTO is seized during a normal wave condition. Results show that the amplitudes of the motion and tether forces of the WEC are not significantly larger than those for normal operating condition (without PTO failure). However, the presence of a PTO seizure modulates the frequency content of the dynamic loading acting on the WEC. The cyclical loading frequency increases by six to seven times when a PTO located on the tether became seized, for the wave case being investigated. The amplitude of the cyclical loading is however decreased. The changes of the dynamic loading behaviour could potentially reduce the fatigue life of the affected WEC components, and hence increased the cost of energy produced using the WEC.

Acknowledgement

This work was supported with supercomputing resources provided by the high-performance computing (HPC) clusters at Sandia National Laboratories and University of California Berkeley. We would also like to thank CalWave Power Technology Inc for their supporting.

Sandia National Laboratories is a multimission laboratory managed and operated by National Technology and Engineering Solutions of Sandia LLC, a wholly owned subsidiary of Honeywell International Inc., for the U.S. Department of Energy's National Nuclear Security Administration under contract DE-NA0003525.

References

[1] IEC TS 62600-2 ED2 (2018). Marine energy – Wave, tidal and other water current converters – Part 2: Design requirements for marine energy systems. 114/243/RR

[2] WES (2016). Structural Forces and Stresses for Wave Energy Devices - Landscaping Study. ARP LS2, Wave Energy Scotland Limited

[3] T. R. Mundon and B. Nair, "Optimization of a Magnetostrictive Wave Energy Converter," Grand Renewable Energy 2014 Proceedings, Tokyo Big Sight, Japan.

[4] J. M. Niedzwecki and S. K. Thampi, "Snap loading of marine cable systems," Applied Ocean Research, vol 13, pp 2-11, 1991. DOI: 10.1016/S0141-1187(05)80035-5

[5] R.G. Coe, V. S. Neary, M.J. Lawson, Y. Yu, and J. Weber, "Extreme Conditions Modeling Workshop Report," Technical Report, NREL/TP-5000-62305-SNL/SAND2014-16384R, 2014.

[6] Bolt Lifesaver Technical Introduction. Accessed Feb. 2019: https://boltseapower.com/technology/bolt-lifesaver-technical-introduction/

[7] K. Ruehl, C. Michelen, S. Kanner, M. Lawson, and Y.-H. Yu, "Preliminary Verification and Validation of WEC-Sim, an Open-Source Wave Energy Converter Design Tool," in Proceedings of the 33rd International Conference on Ocean, Offshore and Arctic Engineering, OMAE 2014, San Francisco, CA, 2014.

[8] J. H. Todalshaug et al., "The NumWEC project. Numerical estimation of energy delivery from a selection of wave energy converters – final report," 2015. DOI: 10.13140/RG.2.1.3807.8885

[9] T. T. Tran and D. H. Kim, "A CFD study of coupled aerodynamic-hydrodynamic loads on a semisubmersible floating offshore wind turbine," Wind Energy, vol. 21, pp. 70–85, 2018, DOI: 10.1002/we.2145

[10] CD-Adapco, 2016. STAR-CCM v.11.02 help manual

[11] Galway Bay Test Site, Accessed in Sep 2018. http://www.oceanenergyireland.ie/Observation/DownloadWave

[12] P. J. Roache, "Perspective: a method for uniform reporting of grid refinement studies," Journal of Fluids Engineering, vol. 116, pp. 405-413, 1994. DOI: 10.1115/1.2910291

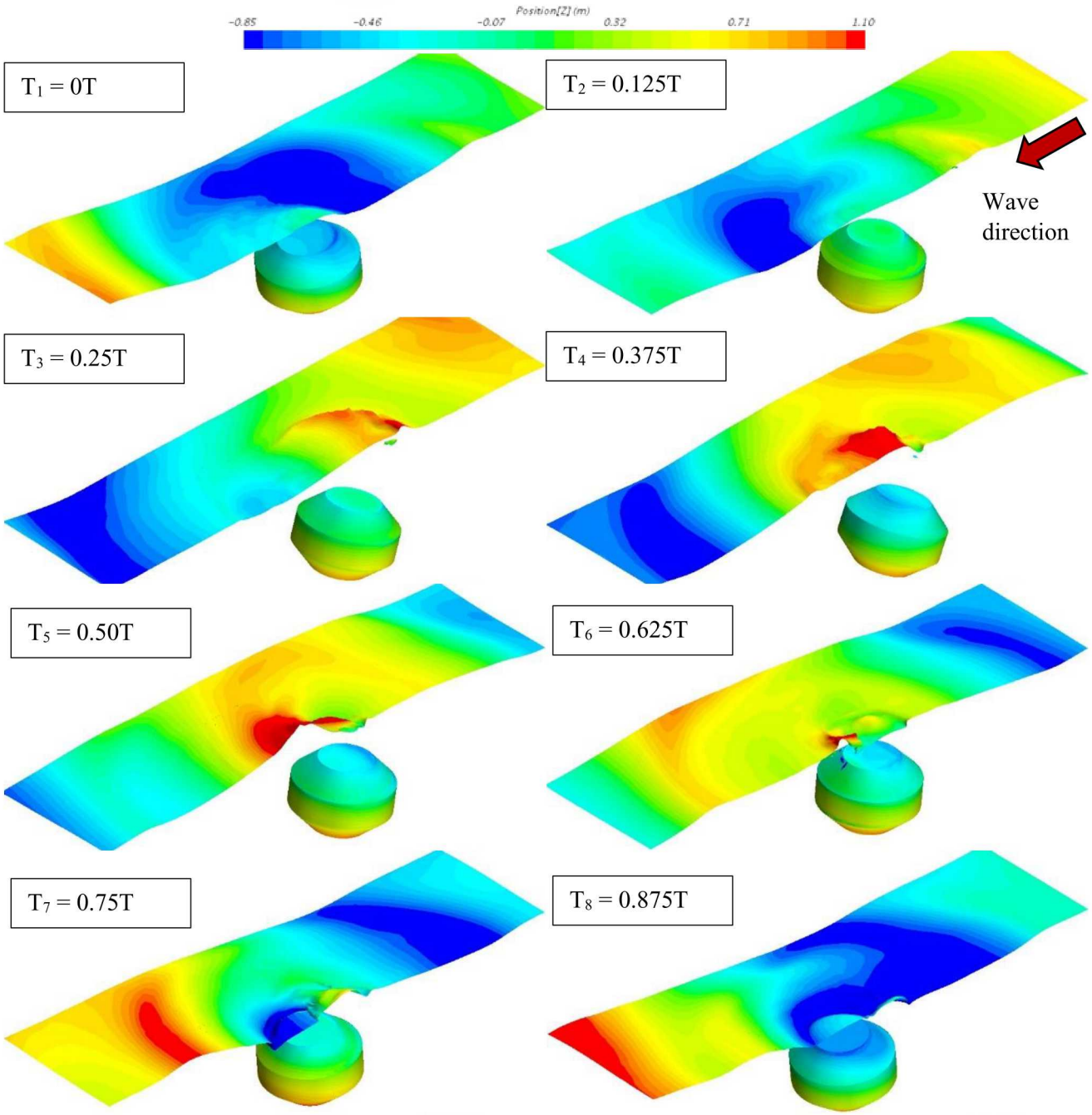

Fig. 10. Instantaneous water surface around submerged WEC body during a period of operational wave condition (0T ÷ 0.875T).